The Astrophysical Journal, 723:1110–1118, 2010 November 10 doi:10.1088/0004-637X/723/2/1110

MIPS 24 μm OBSERVATIONS OF THE HUBBLE DEEP FIELD SOUTH: PROBING THE IR–RADIO CORRELATION OF GALAXIES AT $z > 1$

Minh T. Huynh[1], Eric Gawiser[2], Danilo Marchesini[3], Gabriel Brammer[4], and Lucia Guaita[5]
[1] Infrared Processing and Analysis Center, MS220-6, California Institute of Technology, Pasadena CA 91125, USA; mhuynh@ipac.caltech.edu
[2] Department of Physics and Astronomy, Rutgers University, 136 Frelinghuysen Road, Piscataway, NJ 08854, USA
[3] Department of Physics and Astronomy, Tufts University, Medford, MA 02155, USA
[4] Department of Astronomy, Yale University, New Haven, CT 06520, USA
[5] Departmento de Astronomia y Astrofisica, Universidad Catolica de Chile, Santiago, Chile
Received 2010 June 16; accepted 2010 August 12; published 2010 October 19

ABSTRACT

We present MIPS 24 μm observations of the Hubble Deep Field South taken with the *Spitzer Space Telescope*. The resulting image is 254 arcmin^2 in size and has a sensitivity ranging between ∼12 and ∼30 μJy rms, with a median sensitivity of ∼20 μJy rms. A total of 495 sources have been cataloged with a signal-to-noise ratio greater than 5σ. The source catalog is presented as well as source counts which have been corrected for completeness and flux boosting. The IR sources are then combined with MUSYC optical/NIR and ATHDFS radio observations to obtain redshifts and radio flux densities of the sample. We use the IR/radio flux density ratio (q_{24}) to explore the IR–radio correlation for this IR sample and find $q_{24} = 0.71 \pm 0.31$ for sources detected in both IR and radio. The results are extended by stacking IR sources not detected in the radio observations and we derive an average q_{24} for redshift bins between $0 < z < 2.5$. We find that the high-redshift ($z > 1$) sources have an average q_{24} ratio which is better fit by local LIRG SEDs rather than local ULIRG SEDs, indicating that high-redshift ULIRGs differ in their IR/radio properties. So, ULIRGs at high-redshift have SEDs different from those found locally. Infrared-faint radio sources are examined, and while nine radio sources do not have an MIPS detection and are therefore radio-loud active galactic nuclei (AGNs), only one radio source has an extreme IRAC 3.6 μm to radio flux density ratio indicating it is a radio-loud AGN at $z > 1$.

Key words: galaxies: evolution – galaxies: formation – galaxies: starburst

Online-only material: color figures, machine-readable table

1. INTRODUCTION

The tight correlation between the far-IR and radio emission of star-forming galaxies has been well studied in the local universe and established over many orders of magnitude in luminosity (e.g., Helou et al. 1985; Yun et al. 2001). The radio emission of normal galaxies is dominated by synchrotron radiation from relativistic electrons accelerated by supernovae and free–free emission from H II regions (Condon 1992). Both supernovae and H II regions are related to young, massive stars ($M \gtrsim 10\,M_\odot$), and hence radio emission in normal galaxies is correlated with star formation. The UV emission from young stars is re-radiated by dust in the mid-to-far-infrared so IR emission is also related to star-forming processes. The far-IR/radio correlation is important because it is a probe of the star-forming processes taking place. Deviations from the correlation may occur due to, for example, the varying strength of galactic magnetic fields, evolution of dust and metallicity properties, and increasing inverse Compton losses off the cosmic microwave background (e.g., Murphy 2009; Lacki & Thompson 2010). The far-IR/radio correlation can also be used to select radio loud active galactic nucleus (AGN; e.g., Donley et al. 2005). Thus, it is important to determine whether the correlation holds at high redshift.

A sensitive infrared probe of high-redshift star formation is the 24 μm band of the Multiband Imaging Photometer for *Spitzer* (MIPS) instrument (Rieke et al. 2004) on board the *Spitzer Space Telescope* (Werner et al. 2004). Several deep surveys have correlated 24 μm with radio data to study the mid-IR/radio relation (Boyle et al. 2007; Beswick et al. 2008; Ibar et al. 2008; Garn & Alexander 2009). Some of these authors (Boyle et al. 2007; Beswick et al. 2008) observe a change in the mid-IR/radio ratio at faint radio and/or 24 μm flux densities, but the differences in the results are likely to be because of selection biases which lead to different populations being studied.

More recent work in the COSMOS field has found little variation in the IR–radio ratio of star-forming galaxies for $z < 1.4$, and for the limited sample of sources confirmed at $z > 2.5$ the average IR–radio ratio is still the same as that found locally (Sargent et al. 2010). Discrepant measurements of the average IR–radio ratio can be reconciled by the fact that previous studies selected in either IR or radio, or required a detection in both bands (Sargent et al. 2010).

In 1998, the *Hubble Space Telescope (HST)* observed a region in the southern continuous viewing zone as a complementary observation to the Hubble Deep Field North (HDF-N; Williams et al. 1996). This field, known as the Hubble Deep Field South (HDF-S; Williams et al. 2000), reaches a limit of ∼30 mag in the four *HST* WFPC2 broadband filters. Simultaneous observations with the other *HST* instruments, NICMOS and STIS, reach similarly deep levels in the near-infrared and ultraviolet. In addition to the main *HST* deep fields, a mosaic of nine flanking fields was imaged to shallower levels of ∼25 mag in *I* (*F814W*) (Lucas et al. 2003). Wide-field ground-based imaging has been performed by Palunas et al. (2000) and the Multiwavelength Survey by Yale-Chile (MUSYC) team (Gawiser et al. 2006), reaching *R*-band magnitude limits of ∼25 and 26, respectively. This field has been the target of deep radio observations reaching ∼10 μJy rms at 1.4, 2.5, 5.2, and 8.7 GHz (Huynh et al. 2005, 2007).

Confirming the COSMOS results requires a deep and reasonably wide MIPS field. In this paper, we present the MIPS 24 μm

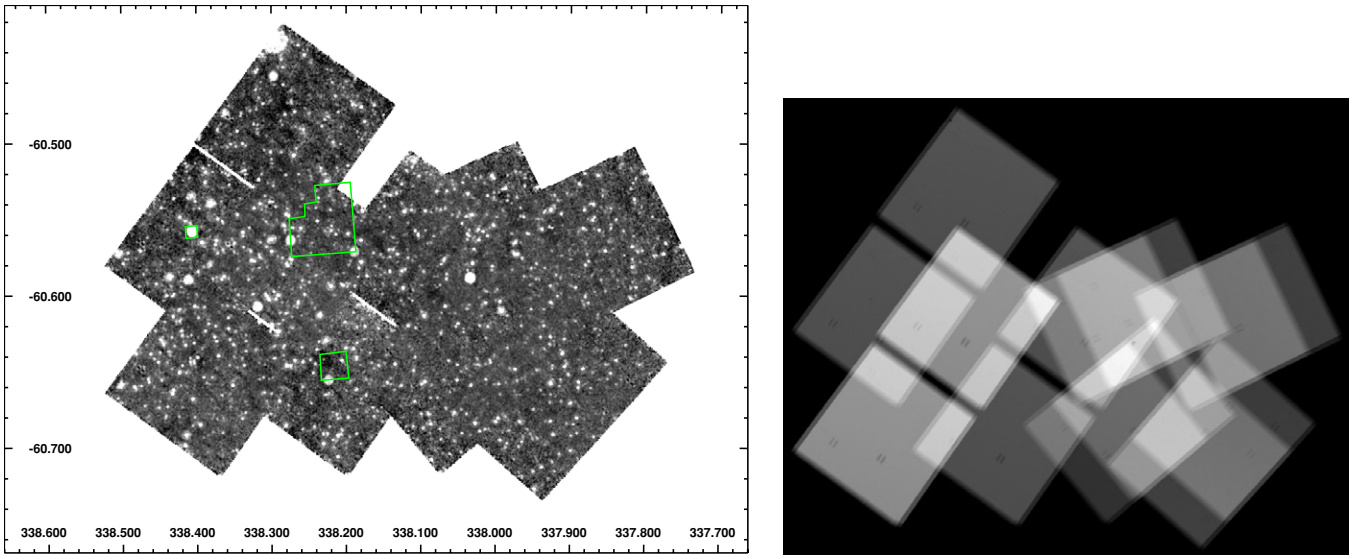

Figure 1. Left: the MIPS 24 μm image of the HDF-S region. The green chevron figure marks the area covered by the original *HST* WFPC2 deep field, the squares to the east and south are the *HST* STIS and NICMOS deep fields, respectively. Right: the coverage map of the MIPS 24 μm image; white indicates most coverage and black indicates no coverage.

(A color version of this figure is available in the online journal.)

observations of the HDF-S and take advantage of the enormous amount of multiwavelength data available to study the IR–radio correlation of galaxies detected in this field. We use a stacking technique in the radio to determine the average IR–radio ratio of a flux-limited IR selected galaxy sample.

In Section 1, we describe the MIPS observations and data reduction. We summarize the multiwavelength data used for this work, in particular the MUSYC data, in Section 2. The MIPS source detection and extraction is discussed in Section 4 and here we present the 24 μm catalog, source counts, and redshift distributions. Section 5 reports our work on the IR–radio correlation in the HDF-S and our identification of infrared-faint radio sources (IFRSs) in the field. We conclude with a summary in Section 6. A Hubble constant of 71 km s^{-1} Mpc^{-1} and a standard Λ-CDM cosmology with $\Omega_{\rm M} = 0.27$ and $\Omega_{\Lambda} = 0.73$ are assumed throughout this paper.

2. MIPS OBSERVATIONS AND DATA REDUCTION

The MIPS 24 μm observations of the HDF-S were carried out over two campaigns. The first was in 2004 as part of the guaranteed time observations (GTOs; PI: Fazio) and the second in 2007 Cycle 3 observations (PID 30873, PI: Labbe). The GTO observations were taken using the MIPS photometry mode and covered six pointings in the HDF-S region. The Cycle 3 observations consisted of four pointings which covered the area west of the WFPC2 field (Figure 1). The coverage (Figure 1) is very uneven, with effective on sky integration time per pixel ranging from about 4500 s in the deepest area to 900 s in the shallow regions.

The basic calibrated data (BCDs) were downloaded from the *Spitzer* Science Center (SSC) archive and were reduced using version 18.1.5 of the MOsaicker and Point source EXtractor (MOPEX) software from the SSC. As recommended, the first frame from each commanded sequence of exposures (i.e., DCENUM = 0) was discarded. Mosaicking the BCDs at this point resulted in latent artifacts. Flat fields were created using the MOPEX routine *flatfield.pl*, which makes a median flat field from a sequence of BCDs. For the GTO data we found that bright sources in the field affected the flat-field generation because of insufficient dithering within the individual astronomical observing requests (AORs) in the GTO data. Therefore, we combined all AORs in the GTO data to reduce the effect of bright sources being counted in the flat-field statistics. All four GTO AORs in 2004 were observed within 4 hr of each other, so combining all of them to make a master flat is reasonable because the instrument flat-field characteristics do not change over such a short timescale. The Cycle 3 observations do not have the dithering issue, and flat fields were generated for each AOR from simply feeding the BCDs of the individual AOR into *flatfield.pl*.

After flat fielding the BCDs the MOPEX task *overlap.pl* was used to level the backgrounds. The BCDs were then mosaicked in the usual way with MOPEX using the default pixel scale of 2.″45 pixel^{-1}. The outlier rejection, which has a default of 5σ, was set to the more aggressive value of 3σ. The resulting image, with units of MJy sr^{-1}, is shown in Figure 1. This image is about 254 arcmin^2 in size.

MIPS calibration assumes the sources have a 10,000 K blackbody spectrum. Galaxies detected at 24 μm generally have a much redder color and, following Shupe et al. (2008), we apply a color correction by dividing by a factor of 0.961.

3. MULTIWAVELENGTH ANCILLARY DATA

The field was observed by the main three instruments on the *HST* in 1998 to depths rivaling that of original HDF in the north (Williams et al. 2000). The *HST* imaging reaches 10σ AB magnitudes of approximately 27.7 in I band ($F814W$) (Casertano et al. 2000) in the deepest region. Including the flanking fields, Hubble imaging covers only a small $\sim$50 arcmin^2 area, however.

More recently, the MUSYC observed an approximate 37 $\times$ 37 arcmin^2 region surrounding the HDF-S in $UBVRIz'$ optical bands (Gawiser et al. 2006). These observations reach $UBVRIz'$ magnitude limits (5σ, AB) of 26.0, 26.1, 26.0, 25.8, 24.7, and 23.6, respectively. The MUSYC team also obtained NIR imaging in J, H, and K' filters reaching 5σ depths of 22.9, 21.8,

Table 1
The MIPS 24 μm Catalog

ID	R.A.	Decl.	$S_{24\,\mu m}$	$dS_{24\,\mu m}$	S/N
MUSYC_MIPSJ223100.6−603403	337.7524414	−60.5674782	882.0	46.2	31.8
MUSYC_MIPSJ223105.6−603357	337.7733459	−60.5657158	355.8	15.0	15.2
MUSYC_MIPSJ223106.3−603421	337.7760620	−60.5725441	719.7	15.1	32.2
MUSYC_MIPSJ223110.7−603126	337.7944946	−60.5239792	717.2	55.2	28.5
MUSYC_MIPSJ223111.0−603518	337.7959290	−60.5884361	205.6	11.3	10.2

(This table is available in its entirety in a machine-readable form in the online journal. A portion is shown here for guidance regarding its form and content.)

and 21.1 Vega magnitudes over two 10 × 10 arcmin^2 fields in the extended HDF-S (Quadri et al. 2007).

Infrared Array Camera (IRAC) data from *Spitzer* was also obtained as part of the GTO (PI: Fazio) and 2007 Cycle 3 observations (PID 30873, PI: Labbe). The BCDs from the SSC archive had the usual procedures applied to remove cosmic rays and artifacts, such as column pulldown, muxbleed, and maxstripe (see Marchesini et al. 2009 for details). Individual background-subtracted images were combined into mosaics covering two 10 × 10 arcmin^2 regions to limiting AB magnitudes (3σ) of 24.5, 24.0, 22.2, and 22.1 at 3.6, 4.5, 5.8, and 8.0 μm, respectively (Marchesini et al. 2009).

Accurate photometric redshifts were determined with EAZY from the MUSYC 14 band optical–IRAC data (Marchesini et al. 2009). EAZY, a template-fitting code similar to HYPERZ (Bolzonella et al. 2000) and BPZ (Benítez 2000), has been found to provide high-quality redshifts over $0 \lesssim z \lesssim 4$ (Brammer et al. 2008), despite the fact that it is not trained on a spectroscopic sample. EAZY has the option of linearly combining templates when fitting sources and provides multiple estimates of the photometric redshift, including $z_{\rm peak}$, which is determined from the full probability distribution rather than a straight χ^2 minimization. In the case where there are two widely separated peaks in the redshift probability function, $z_{\rm peak}$ selects the peak with the largest integrated probability. In the eCDFS, the MUSYC team achieved photometric redshift accuracies of $\delta z/(1+z) \sim 0.008$ with EAZY, but this result came from supplementing *UBV RIz′ JHK* optical imaging, with *Spitzer* IRAC and 18 medium-band optical images from Subaru (Cardamone et al. 2010). The photometric redshifts from the 14 band optical–IRAC data have an accuracy of $\delta z/(1+z) = 0.000 \pm 0.033$ and the fraction of catastrophic outliers is only 4% (Marchesini et al. 2009).

The radio observations of the HDF-S were made between 1998 and 2001 with the Australia Telescope Compact Array using all four available frequency bands. Between 100 and 300 hr of observing at each band yielded images at 1.4, 2.5, 5.2, and 8.7 GHz with maximum sensitivities of ∼10 μJy rms (Huynh et al. 2005, 2007).

4. MIPS IMAGE ANALYSIS

4.1. Source Detection and Extraction

Source detection and extraction were performed using the Astronomical Point Source extraction (APEX) tools in the MOPEX software. First, APEX performs a local background subtraction by taking a median within a box surrounding each pixel. The box size was set to 34 pixels, or ∼14 times the FWHM of the 24 μm point-spread function, and the median calculated after rejecting the 100 highest pixels. APEX detects sources when a pixel cluster has values which are above the noise threshold, but this requires a good estimate of the noise. The MOPEX and APEX software can produce several types of noise images. The "std" noise image produced at the mosaicking stage provides the empirical scatter of each pixel from the repeated observations divided by the square-root of the number of observations. This underestimates the true noise because it does not account for pixel-to-pixel correlated noise or confusion noise. APEX generates an output "noise" map by calculating the noise within a local box, and here we use the same settings as for the background subtraction—34 pixel rectangular box and rejection of 100 outlier pixels. Using an approach similar to Frayer et al. (2009), the "std" and "noise" images are then combined in quadrature with equal weights to obtain a combined uncertainty image for source detection and extraction.

We then checked whether the combined uncertainty image was reasonable by checking this against an independent total noise value. An independent estimate of the total noise in the image was made by measuring the flux density in apertures randomly placed on the image and calculating the standard deviation of the measurements. Two hundred apertures were placed randomly in 60 × 60 pixels regions of a residual image with bright sources removed. The standard deviation of the flux density measurements agreed with the combined uncertainty image to within 50%.

Sources were detected by APEX if they had a peak with a signal-to-noise ratio (S/N) greater than 4 and were fitted using the point-source response function image provided by the SSC. The sources were then included in the final catalog if they had a fitted S/N greater than 5. This relatively high S/N was chosen to minimize the number of spurious detections. Even with this S/N ratio the initial source list (504 total) was visually examined for potential spurious sources such as those in the Airy rings of bright sources. Only nine (∼2%) sources were removed, suggesting that the APEX algorithm is reliable. The final 24 μm catalog contains 495 sources.

The full 5σ catalog is presented in Table 1. A description of the table is as follows.

Column 1: source ID.

Column 2: right ascension in J2000.

Column 3: declination in J2000.

Column 4: 24 μm flux density in μJy.

Column 5: 24 μm flux density uncertainty in μJy. This is the formal error from APEX.

Column 6: S/N of the source.

4.2. Completeness and Flux Boosting

The completeness of the source catalog was estimated by simulations. Monte-Carlo-like simulations were performed by injecting 10,000 sources at random locations onto the map and extracting them using the same technique as adopted for the production of the catalog. While completeness levels vary

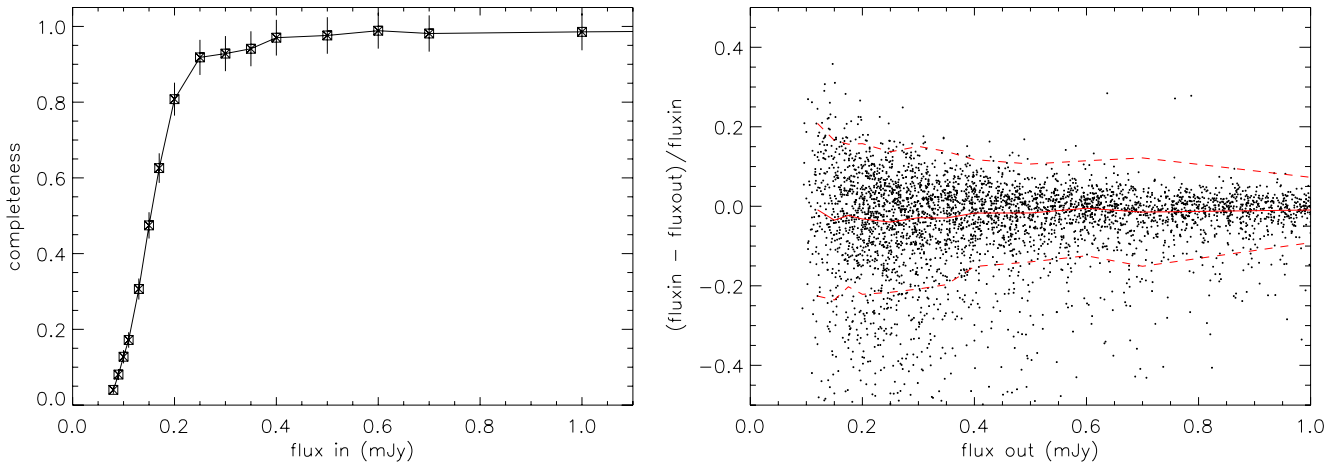

Figure 2. Left: completeness as a function of input flux density, as derived from the Monte Carlo simulations. Completeness is the number of extracted sources divided by number of input sources. Right: the distribution of (input flux density − output flux density)/input flux density as a function of output flux density for the simulated sources. The solid red line is the mean of the simulation and the dashed lines mark the 1σ upper and lower bounds.

(A color version of this figure is available in the online journal.)

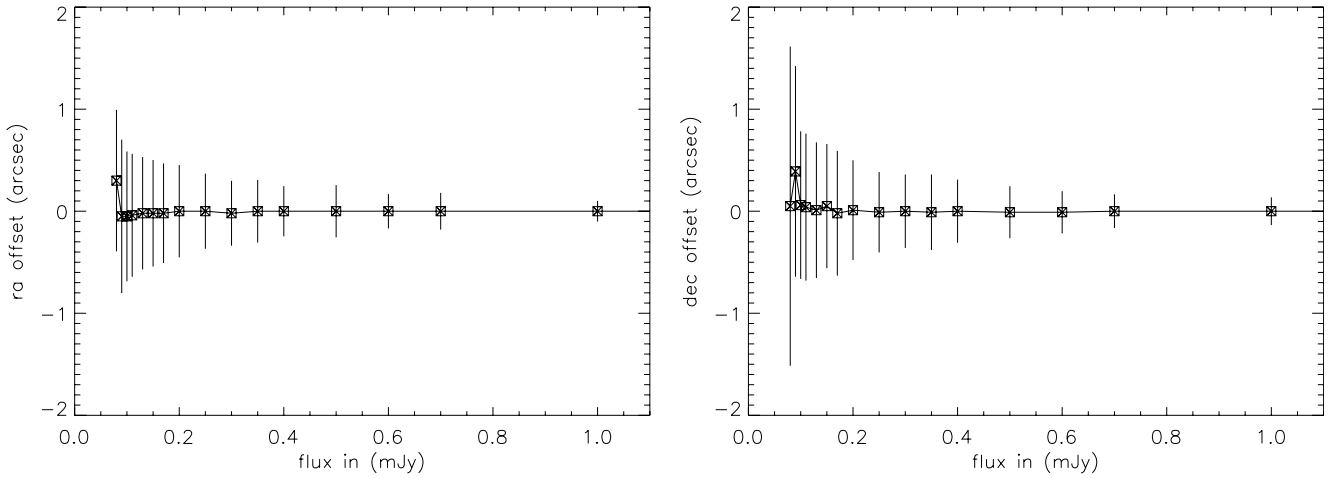

Figure 3. Offset in R.A. (left) and decl. (right) between the recovered positions of sources in the simulation and the true input positions, as a function of input flux density. The error bars mark the 1σ uncertainty in the position as a function of input flux density.

significantly across the image as a function of coverage and flux density, we can recover the overall completeness level of the generated catalog by injecting sources over the full image. A single source was injected per simulation, and the input flux density varied from 50 to 3000 μJy to sample the full range of interest. The completeness as a function of flux density is shown in Figure 2. The completeness rises steeply from about 10% at 100 μJy to approximately 90% at 250 μJy. The 50% completeness level occurs at approximately 150 μJy.

Source detection algorithms that rely on finding a peak above a local noise background lead to flux boosting. This is because sources that lie on a noise peak have their flux density increased and therefore have a higher probability of being detected, while sources which lie on a noise trough have decreased flux densities and may be excluded altogether. This effect is most pronounced in the faintest flux density bins, i.e., in sources with an S/N close to the limit of the catalog. The degree of flux boosting can be estimated by examining the output to input flux density of the simulations (Figure 2). We find that flux densities are boosted by about 1%–4% for measured flux densities of 100–300 μJy, on average. The flux boosting is negligible for sources with true flux densities brighter than 300 μJy.

The simulations can also be used to gauge the positional accuracy of the catalog by comparing input and output positions. The median of the R.A. and decl. offsets are plotted for various input flux density bins in Figure 3. The positional accuracy can be estimated from the standard deviation in the offsets of each of these bins. We find that at the faintest levels (80 μJy) the R.A. and decl. uncertainties are approximately 0.8 and 1.3 arcsec, respectively. The positional accuracy is much better than 0.5 arcsec for sources that are 1 mJy and brighter. This is the random component only and does not take into account any systematic offsets in the pointing. *Spitzer* has an absolute pointing uncertainty of about 1 arcsec.

5. RESULTS

5.1. Source Counts

The source counts were derived from the S/N $\geqslant$ 5 catalog. We correct the source counts for flux boosting and completeness using the results of Section 4.2. Figure 4 shows the Euclidean normalized source counts ($dN/dS \times S^{2.5}$) and the results are tabulated in Table 2. The uncertainties listed are derived from Poissonian statistics. The counts from this work span the peak near 0.2–0.3 mJy. We have also plotted the counts from five GTO fields (Papovich et al. 2004), the FIrst Look Survey (FLS) field (Marleau et al. 2004), and the Spitzer Wide-field InfraRed Extragalactic (SWIRE) fields (Shupe et al. 2008) for

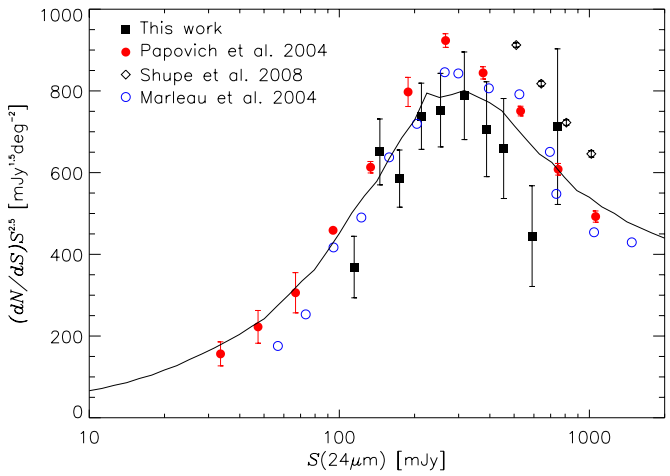

Figure 4. Euclidean normalized differential 24 μm source counts in the HDF-S (black squares). These counts have been corrected for incompleteness and flux boosting as described in Section 4.2. The solid line shows the prediction from the model by Lagache et al. (2004). Counts from other deep surveys in the literature are plotted for comparison.

(A color version of this figure is available in the online journal.)

comparison. In the fainter bins, HDF-S counts are broadly consistent with that from the previous work, showing the steep decline for $S_{24} < 0.2$ mJy. At brighter flux densities the counts are consistent with the FLS, within the uncertainties, but lower than that from the GTO or SWIRE fields. At ∼0.5 mJy the SWIRE counts are about 40% higher the HDF-S and about 20% higher than the FLS or GTO source counts. This illustrates that there is significant field-to-field variation, which Shupe et al. (2008) estimated to be about 10% for sub-mJy flux densities in regions as large as the SWIRE fields (>7°).

Also overlaid on Figure 4 are the normalized counts from the model of Lagache et al. (2004). See Lagache et al. (2004) for details; in brief, this model uses starburst and normal galaxy templates and fits for the evolution of the local luminosity function that is best constrained by observed source counts and redshift distributions. We note that this model used counts at 15, 60, 170, and 850 μm from the literature as well as the 24 μm counts from Papovich et al. (2004). The model is broadly consistent with the HDF-S, FLS, and GTO counts and reproduces the turnover at ∼0.1 mJy that is seen in these fields.

5.2. Optical Counterparts

We used the MUSYC catalogs to identify optical counterparts to the MIPS sources and obtain redshift information from either the spectroscopic or photometric catalogs. The MUSYC imaging overlaps almost the entire MIPS imaging, with only the ∼ 24 arcmin^2 region north of decl. = −60.4994 falling outside the MUSYC observations. Thus, 25/495 (5%) MIPS sources do not have MUSYC coverage. The MUSYC *K*-selected catalog (Quadri et al. 2007) and v1.0 optical catalog (Gawiser et al. 2006) were searched for counterparts to the rest of the MIPS sample.

With the ∼1 arcsec seeing of the observations and the astrometric uncertainties of the USNO-A2 stars used for astrometry, the positional uncertainties of the MUSYC sources are about 0.2–0.3 arcsec. For MIPS the 1σ positional uncertainty can be estimated by $0.5\theta_{\rm FWHM}/$ (S/N) assuming Gaussian noise, and hence a beam size of 6 arcsec implies a positional uncertainty of 0.6 arcsec (in each coordinate) for the faintest sources. Including the *Spitzer* 1 arcsec absolute pointing uncertainty, the 1σ offset between MIPS and MUSYC sources should be about 1.3 arcsec for the faintest MIPS sources.

Table 2
The MIPS 24 μm Source Count for Hubble Deep Field South

Range in $S_{24\,\mu m}$ (μJy)	$\langle S_{24\,\mu m}\rangle$ (μJy)	N	Corrected N	$(dN/dS)S^{2.5}$ (mJy$^{1.5}$ deg^{-2})
110–134	115	24	121.4	368.8 ± 75.3
134–163	145	65	149.4	650.7 ± 80.7
163–198	174	70	106.8	585.4 ± 70.0
198–241	213	83	97.5	738.0 ± 81.0
241–293	254	70	76.0	753.0 ± 90.0
293–356	316	54	58.0	788.1 ±107.2
356–433	388	37	38.4	706.3 ± 116.1
433–526	454	29	29.7	659.0 ± 122.4
526–640	590	13	13.2	444.6 ± 123.3
640–779	746	14	14.3	712.5 ± 190.4

Notes. N is the raw number of galaxies in the bin, and corrected N is the number corrected for incompleteness. The median flux density of the bin, $\langle S_{24\,\mu m}\rangle$, has been corrected for flux boosting.

Figure 5 shows a plot of distribution of the offsets between all MIPS and MUSYC *K*-selected (Quadri et al. 2007) sources within 2 arcsec. As expected, there is a peak in the distribution of offsets at $\lesssim$0.5 arcsec. The contribution from chance matches due to the optical source density is also shown in Figure 5. We find that the number of chance matches meets the number of observed matches at a radius of ∼1.5 arcsec and therefore use this as our matching radius. Three hundred sixty-nine MIPS sources have a counterpart in the *K*-selected catalogs and a photometric redshift from Marchesini et al. (2009). A further 37 have counterparts in the optical MUSYC catalogs, which cover a larger area than the *K*-band imaging. For these 37 sources EAZY photometric redshifts were calculated from the MUSYC *UBVRIz* optical data plus a narrowband 5000 Å image. A comparison of these seven-band photometric redshifts with 166 spectroscopic redshifts from the literature finds only 18% have $\delta z/(1+z) > 0.2$. Excluding these outliers, we find $\delta z/(1+z) = 0.027 \pm 0.046$, and thus conclude that the photometric redshifts are statistically reliable. In total 406/495 (82%) of the MIPS sources have a MUSYC optical or NIR counterpart. Three have more than one MUSYC source within 1.5 and in these cases the optical candidates were individually examined and the most likely candidate chosen using the P statistic (e.g., Downes et al. 1986; Lilly et al. 1999).

Spectroscopic redshifts from the literature are available for 22 of the MIPS sources, and we assume the photometric redshift, where available, for the remaining sources. The redshift distribution of the MIPS sources peak at $z \sim 0.5$ with a tail to high redshift ($z > 2$; Figure 5). The total infrared luminosity (8–1000 μm) of the sources is estimated by fitting the 24 μm flux density to the luminosity-dependent spectral energy distribution (SED) templates of Chary & Elbaz (2001). We integrate the best-fit template over 8–1000 μm to derive the total IR luminosity (LIR; Figure 6). We find that luminous IR galaxies (LIRGS; $10^{11}\,L_\odot < \mathrm{LIR} < 10^{12}\,L_\odot$) are detected out to $z \sim 1.1$, while ultraluminous IR galaxies (ULIRGs; LIR > $10^{12}\,L_\odot$) are detected out to higher redshifts. We note that while the Chary & Elbaz (2001) templates exhibit observed FIR flux density ratios which are more representative of $z \sim 1$ galaxies than Dale & Helou (2002) or Lagache et al. (2003) templates (Magnelli et al. 2009), the choice of templates can lead to ∼0.3 dex variation

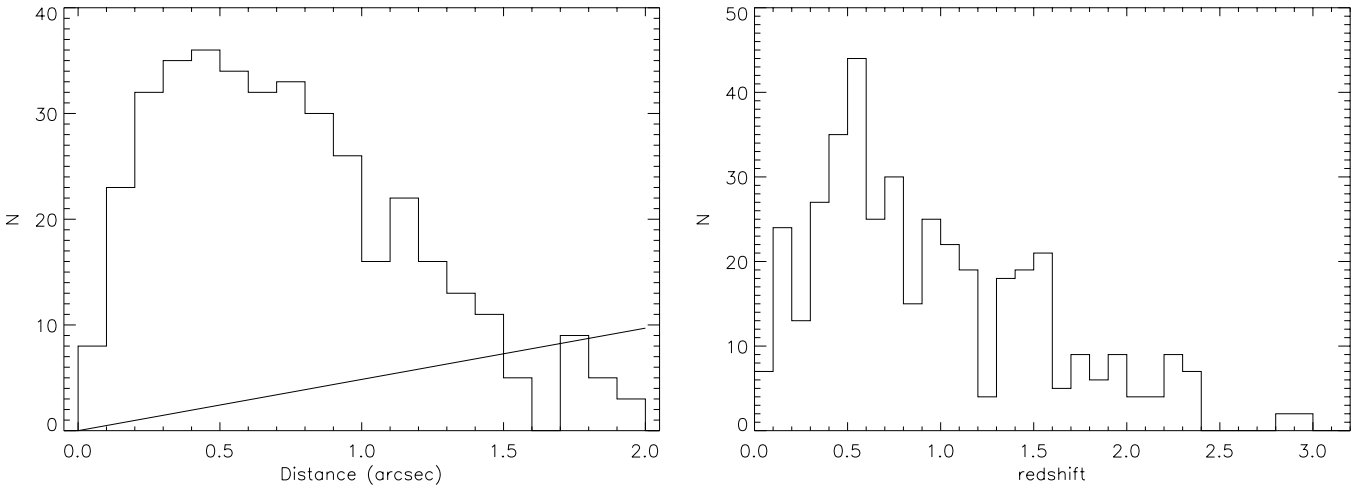

Figure 5. Left: histogram of the total offsets between the MUSYC optical candidate and the 24 μm source. Most MIR sources have an optical counterpart within 1 arcsec. The solid line is the expected number of coincident sources with the same offset, assuming the MUSYC source density of 56 arcmin^{-2}. Right: the redshift distribution of the 406 MIPS sources in HDFS with a MUSYC optical counterpart. There are spectroscopic redshifts for 22 sources.

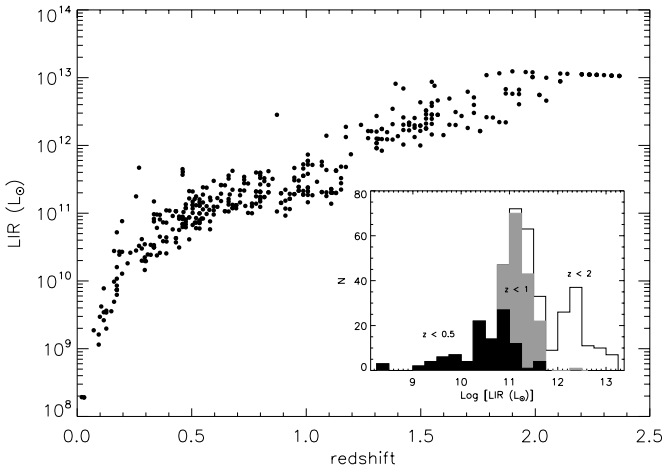

Figure 6. Total IR luminosities of the 358 MIPS sources with redshift information. They were derived by fitting to the luminosity-dependent SEDs of Chary & Elbaz (2001). Inset shows the corresponding LIR histograms of the sample for $z < 0.5$ (black), $z < 1$ (gray), and $z < 2$ (white).

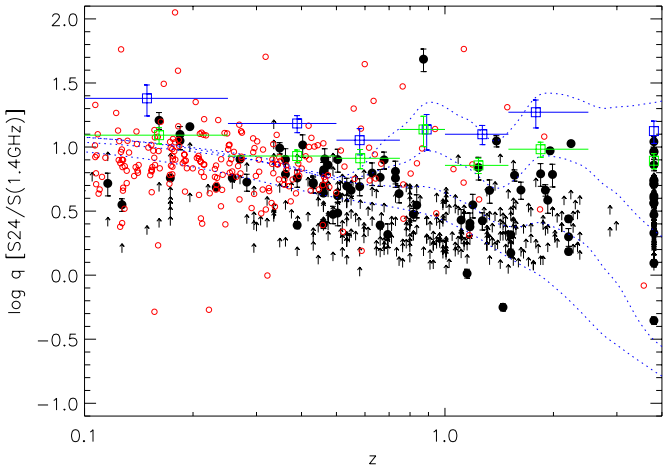

Figure 7. Observed 24 μm vs. radio flux density ratio (q_{24}) as a function of redshift. HDFS sources detected in MIR and radio are marked as black circles. MIR only sources not detected in the radio are plotted as lower limits assuming the conservative radio detection limit of 100 μJy. Sources with no redshift information are plotted at $z = 3.8$. Red circles are results from the xFLS (Frayer et al. 2006). The blue squares are average q_{24} for the MIR sources undetected in the radio, where the average radio flux density is derived from a stacking analysis. The green squares are the average q_{24} for all MIR sources, i.e., combining the blue squares with radio detections. The dotted blue lines are SED tracks from Chary & Elbaz (2001) for galaxies with total infrared luminosities of 10^9, 10^{11}, 10^{12}, and 10^{13} $L_\odot$, going from top to bottom.

(A color version of this figure is available in the online journal.)

in luminosity. Fitting to the 24 μm flux density alone can give a good LIR estimate up to about $z \sim 1.4$, but for $1.4 < z < 2.5$ the LIR can be overestimated by up to a factor of 4 (Murphy et al. 2009).

6. DISCUSSION

6.1. Infrared–Radio Correlation

Radio counterparts to the MIR sources were obtained using the 1.4 GHz radio catalog of the HDF-S (Huynh et al. 2005). We applied a simple radial match of 3 arcsec and find that 84 MIPS sources have a radio counterpart. The matching distance is large enough for obtaining bona fide matches since the 24 μm positional uncertainties are $\sim$1.2 arcsec and the radio positions are better than about 1 arcsec in most cases (Huynh et al. 2005). The P statistic suggests the probability of one or more radio sources within 3 arcsec of an IR one by chance is $\sim$0.3%, but this estimate does not take into account the individual positional uncertainties and assumes the radio source population is not clustered.

The IR/radio correlation as a function of redshift is presented in Figure 7, shown as the observable parameter $q_{24} = \log(S_{24\,\mu\mathrm{m}})/S_{1.4\,\mathrm{GHz}})$. For the 84 sources with detections in both the IR and radio the median $q_{24} = 0.71 \pm 0.31$. This is consistent with the $q_{24} = 0.84 \pm 0.28$ found in the xFLS Appleton et al. (2004) and $q_{24} = 0.66 \pm 0.39$ in the Subaru *XMM-Newton* Deep Field (Ibar et al. 2008). Overlaid on Figure 7 are SED tracks from local templates by Chary & Elbaz (2001). We find that up to redshift one the IR sources appear to follow tracks of local SEDs, suggesting the IR–radio correlation holds to this redshift. Above redshift one the 24 μm band starts to observe the MIR regime ($\lesssim$12 μm rest frame) where polycyclic aromatic hydrocarbon (PAH) emission and silicate absorption strengths vary widely in individual galaxies, and hence a wide range of MIR/radio ratios is possible. The high-redshift ($z > 1$) sources in Figure 7 also fall within the ratios allowed by local templates, but most are best described by the SEDs of relatively low

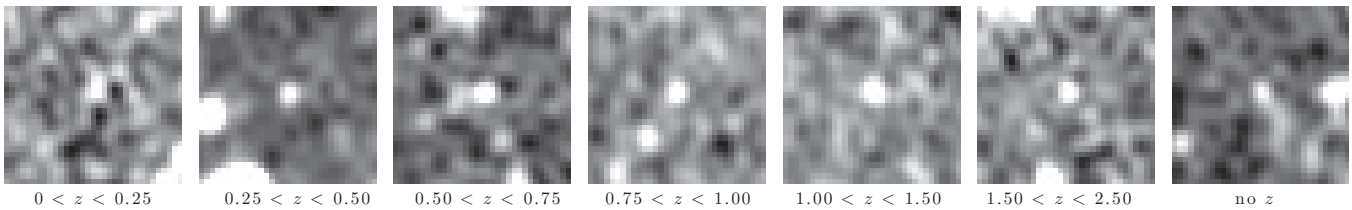

Figure 8. Postage stamps of the radio stacks of MIPS sources for the redshift bins as shown. The stacks are 1 × 1 arcmin^2 in size. In all cases, there is a significant radio flux at the center of the stack, which is reported in Table 3.

Table 3
Summary of Radio Stacking Results of MIPS Sources

z	Median z	$N_{\rm det}$	$N_{\rm stack}$	Stacked $S_{1.4\,\rm GHz}$ (μJy)	Stacked q_{24}	Average q_{24}
$0 < z < 0.25$	0.149	8	25	15.2 ± 4.1	$1.38^{+0.10}_{-0.14}$	$1.09^{+0.06}_{-0.07}$
$0.25 < z < 0.50$	0.389	19	54	23.8 ± 3.5	$1.18^{+0.06}_{-0.07}$	$0.93^{+0.05}_{-0.05}$
$0.50 < z < 0.75$	0.580	14	65	22.8 ± 5.2	$1.05^{+0.09}_{-0.11}$	$0.91^{+0.07}_{-0.08}$
$0.75 < z < 1.00$	0.890	3	57	16.4 ± 5.0	$1.14^{+0.12}_{-0.16}$	$1.14^{+0.10}_{-0.14}$
$1.00 < z < 1.50$	1.270	10	72	18.2 ± 3.0	$1.11^{+0.07}_{-0.08}$	$0.86^{+0.06}_{-0.06}$
$1.50 < z < 2.50$	1.787	13	61	12.0 ± 2.9	$1.27^{+0.10}_{-0.12}$	$0.98^{+0.05}_{-0.06}$
No redshift	···	16	73	18.7 ± 3.6	$1.12^{+0.08}_{-0.10}$	$0.89^{+0.06}_{-0.06}$

Notes. $N_{\rm det}$ is the number of MIPS sources in each bin which is detected in the radio image. $N_{\rm stack}$ is the number of MIPS sources not detected in the radio image and therefore the number stacked in this analysis, resulting in the stacked $S_{1.4\,\rm GHz}$ listed in Column 5. Stacked q_{24} is the IR–radio flux density ratio for the stacked sample. Average q_{24} is the IR–radio flux density ratio for all MIPS sources in the redshift bin, obtained by combining the detections with the stacked results.

luminosity SEDs ($L < 10^{12}\ L_\odot$). These sources have luminosities that are ULIRG-like ($>10^{12}\ L_\odot$; Figure 6) but exhibit ratios similar to local $\sim 10^{11}\ L_\odot$ LIRGs, implying that the SEDs of high-redshift ULIRGs differ to that of local ones. We speculate that these ULIRGs have strong PAH emission, as seen in other IR samples of high-redshift ULIRGs (e.g., Yan et al. 2007), but IR spectra are needed to confirm that hypothesis.

To extend the results we stack the IR sample in the radio data. First, the IR sources were binned into six redshifts bins, as shown in Table 3. For each redshift bin, the radio data were stacked at positions of all undetected sources and a noise-weighted mean image was produced. Stacks of width 60″ wide were produced and the photometry performed by fitting a point source to the stacked radio image. All stacks, shown as postage stamps in Figure 8, have a significant detection. The resulting q_{24} values from the stacked radio flux densities are shown as blue squares in Figure 7. They have been combined with the actual detections to derive an average q_{24} for all MIPS sources in the various redshift bins (green squares). We find that the average observed q_{24} at high redshift ($z > 1$) is approximately 0.86 (Table 3) and this is consistent with local LIR $\sim 10^{11}$ LIRG SED (Figure 7). At these redshifts our samples have ULIRG luminosities or greater, so this is further evidence that the average IR luminous galaxy at high redshift is better described by a lower luminosity local template. This result is consistent with complementary studies which have found that some high-redshift IR luminous galaxies have cooler SEDs than local galaxies of similar luminosities (Seymour et al. 2010; Muzzin et al. 2010).

As mentioned before, the high-redshift ULIRGs may exhibit stronger PAH emission than local galaxies, leading to a greater q_{24} then expected from local SEDs. However, the increased q_{24} at high redshift may also result from suppressed radio emission. If a galaxy has just begun a burst of star formation then the MIR dust emission may be enhanced due to star formation but the supernova rate, which powers the radio emission, lags the star formation by about ∼30 Myr (the approximate lifetime of 8 $M_\odot$ stars). It is possible that some of the sources at high redshift are nascent starbursts. Increased inverse Compton scattering of the cosmic microwave background at high redshift can lead to lower radio emission than in the local universe, and since the energy density of the CMB scales as $(1 + z)^4$ this could be significant at high redshifts. Another potential explanation is that the high-redshift galaxies have lower magnetic field strengths than local galaxies, leading to decreased electron confinement and therefore lower radio emission.

6.2. *Infrared-faint Radio Sources*

IFRSs are a class of radio sources recently discovered in the Australia Telescope Large Area Survey by Norris et al. (2006). These are radio sources brighter than a few hundred μJy at 1.4 GHz which have no observable infrared counterpart in the *Spitzer* Wide-area Infrared Extragalactic Survey (SWIRE; Lonsdale et al. 2004). Most have flux densities of a few hundred μJy at 1.4 GHz, but some are as bright as 20 mJy, resulting in extreme infrared to radio ratios. Recent very long baseline interferometry detections have constrained the radio sources sizes to less than 0.03 arcsec, suggesting IFRSs are compact AGNs (Norris et al. 2007; Middelberg et al. 2008). Deeper *Spitzer* legacy survey data in the extended Chandra Deep Field South yielded two IRAC detections of the four IFRSs in that field, and SED modeling of these sources with the new constraints showed that they are consistent with $z > 1$ radio-loud AGNs (Huynh et al. 2010).

The MIPS data of the HDF-S allow us to search for IFRSs in this field. There are nine ATHDFS sources with $S_{1.4\,\rm GHz} > 200\,\mu$Jy that do not have an MIPS counterpart. These are listed in Table 4 along with their MIPS (5σ) limit and IRAC properties. All of these sources have low q_{24} values consistent with radio-loud AGNs, and most have moderate photometric redshifts of $0.417 < z < 1.548$. Most are also relatively bright in the IRAC channels and would have been detected by SWIRE depth IRAC imaging. Of the nine sources, one

Table 4
Summary of Radio Sources that have No MIPS 24 μm Counterpart and Hence are Candidate Infrared-faint Radio Sources

Radio ID	$S_{24\,\mu m}$ limit (5σ, μJy)	$S_{1.4\,GHz}$ (mJy)	$S_{3.6\,\mu m}$ (μJy)	$q24$	$S_{1.4\,GHz}/S_{3.6\,\mu m}$	z_{phot}	$\alpha_{1.4\,GHz}^{2.5\,GHz}$[a]
ATHDFS_J223224.5−604113	130	4.108	112	< -1.50	37	0.746	-0.48 ± 0.02
ATHDFS_J223245.6−603857	100	0.843	31.2	< -0.93	27	1.548	-0.69 ± 0.06
ATHDFS_J223205.9−603857	70	0.254	< 2	< -0.56	>127	... [b]	-0.80 ± 0.29
ATHDFS_J223350.0−603741	80	0.670	156	< -0.93	4.4	0.645	-0.36 ± 0.05
ATHDFS_J223232.8−603737	65	0.645	92.6	< -1.00	7.0	1.13	-0.51 ± 0.08
ATHDFS_J223350.5−603503	110	1.252	>4[c]	< -1.06	<310[c]	0.417	-0.85 ± 0.05
ATHDFS_J223258.5−603346	95	1.010	21.31	< -1.03	47.4	...	-0.65 ± 0.05
ATHDFS_J223308.6−603251	75	0.821	101	< -1.04	8.1	0.746	-0.86 ± 0.03
ATHDFS_J223113.5−603147	115	0.831	... [d]	< -0.86	... [d]	... [b]	...

Notes. Only ATHDFS_J223205.9−603857 is faint enough at 3.6 μm to meet the original IFRS definition of Norris et al. (2006). All of these sources have q_{24} values suggestive of radio-loud AGNs. The 3.5 μm data are from Marchesini et al. (2009).
[a] Radio spectral indices are from Huynh et al. (2007) and $S \propto \nu^{\alpha}$.
[b] Not detected in MUSYC optical imaging.
[c] IRAC image of source has artifacts, so photometry is inaccurate.
[d] Out of IRAC coverage.

(ATHDFS_J223205.9−603857) is not in the 5σ IRAC catalog of Marchesini et al. (2009) and one is not in the IRAC field. Hence, only one source matches the Norris et al. (2006) criteria for IFRS. One IFRS in the 252 arcmin^2 MIPS HDF-S region is consistent with the IFRS source density of $\sim$16 deg^{-2} in the eCDFS. ATHDFS_J223205.9−603857 has a $S_{3.6\,\mu m}$ (5σ) limit of 2 μJy and hence a radio-to-IRAC flux density ratio ($S_{1.4\,GHz}/S_{3.6\,\mu m}$) greater than about 130. Similarly high radio-to-IRAC flux density ratios are found for both IFRS and high-redshift radio galaxies (Seymour et al. 2007; Huynh et al. 2010), suggesting they are high-redshift AGNs. For ATHDFS_J223205.9−603857, the low value of $q24$ (< -0.50) and high value of $S_{1.4\,GHz}/S_{3.6\,\mu m}$ therefore suggest that it is a high-redshift ($z > 1$) radio-loud AGN.

The radio spectral index between 1.4 and 2.5 GHz for these nine ATHDFS sources is also listed in Table 4. All but two have radio SEDs with a spectral index $\alpha \sim -0.8$ ($S \propto \nu^{\alpha}$), which is consistent with synchrotron emission. The IFRS candidate ATHDFS_J223205.9−603857 has a spectral index $\alpha = -0.80 \pm 0.29$. This result is consistent with Middelberg et al. (2010) who find IFRSs have $\alpha < -0.7$.

7. SUMMARY

We have presented the MIPS 24 μm observations of the HDF-S from the *Spitzer Space Telescope*. This new MIR image, 250 arcmin^2 in area, reaches a maximum sensitivity of $\sim$12 μJy rms, with the bulk of the image achieving $\sim$20 μJy rms. A catalog of sources brighter than 5σ was compiled, comprising 495 sources. The completeness corrected and flux-deboosted 24 μm source count was presented, and while the counts are consistent with results in the literature they show that there is significant field-to-field variation.

The MIPS sources were matched to MUSYC photometric redshift and ATHDFS 1.4 GHz radio catalogs. The IR–radio ratio q_{24}, $\log(S_{24\,\mu m})/S_{1.4\,GHz})$, for 84 sources with both IR and radio detections has a median $q_{24} = 0.71 \pm 0.31$, consistent with previous results. We find that while there is diversity in galaxy SEDs, the IR–radio correlation appears to hold out to $z \sim 1$. The results were extended by splitting the sample into redshift bins and stacking all IR sources not detected in the radio to derive an average radio flux density and hence an average q_{24}. The observed average q_{24} was compared with that expected from local SED templates and at $z > 1$ the observed average q_{24} is found to be better described by LIRG templates, even though these sources have ULIRG-like luminosities. This is further evidence that the average IR luminous galaxy at high redshift is better described by a lower luminosity local template. The change in q_{24} may be due to enhanced MIR emission, possibly from hot dust heated by AGNs or relatively bright PAH emission, or suppressed radio emission due to lower strength magnetic fields, inverse Compton scattering off the CMB. Several of the high-redshift galaxies may be nascent starburst where the radio emission from supernovae is delayed compared to the IR and hence a high q_{24} results. More detailed IR observations and spectroscopy to determine the AGN/SB nature of the IR galaxies are required to differentiate between these possible scenarios.

The *Herschel Space Observatory*, launched in 2009 May, is currently undertaking deep IR surveys in bands ranging from 70 to 450 μm. These bands are close to the peak of the IR emission from dust and not significantly affected by AGNs or PAH emission. With its unprecedented depth and resolution, *Herschel* will observe large complete samples of IR galaxies to redshifts of $z = 2$ and beyond. In combination with upcoming radio facilities such as eVLA, ASKAP, and MeerKAT, this will allow a major improvement in the study of the IR–radio correlation in the high-redshift universe.

M.T.H. thanks D. Frayer for useful discussions. This work is based in part on observations made with the *Spitzer Space Telescope*, which is operated by the Jet Propulsion Laboratory, California Institute of Technology under a contract with NASA. Support for this work was provided by NASA through an award issued by JPL/Caltech. This material is also based on work supported by the National Science Foundation under grant AST-0807570.

REFERENCES

Appleton, P. N., et al. 2004, ApJS, 154, 147
Benítez, N. 2000, ApJ, 536, 571
Beswick, R. J., Muxlow, T. W. B., Thrall, H., Richards, A. M. S., & Garrington, S. T. 2008, MNRAS, 385, 1143
Bolzonella, M., Miralles, J., & Pelló, R. 2000, A&A, 363, 476
Boyle, B. J., Cornwell, T. J., Middelberg, E., Norris, R. P., Appleton, P. N., & Smail, I. 2007, MNRAS, 376, 1182
Brammer, G. B., van Dokkum, P. G., & Coppi, P. 2008, ApJ, 686, 1503

Cardamone, C. N., et al. 2010, ApJS, 189, 270
Casertano, S., et al. 2000, AJ, 120, 2747
Chary, R., & Elbaz, D. 2001, ApJ, 556, 562
Condon, J. J. 1992, ARA&A, 30, 575
Dale, D. A., & Helou, G. 2002, ApJ, 576, 159
Donley, J. L., Rieke, G. H., Rigby, J. R., & Pérez-González, P. G. 2005, ApJ, 634, 169
Downes, A. J. B., Peacock, J. A., Savage, A., & Carrie, D. R. 1986, MNRAS, 218, 31
Frayer, D. T., et al. 2006, AJ, 131, 250
Frayer, D. T., et al. 2009, AJ, 138, 1261
Garn, T., & Alexander, P. 2009, MNRAS, 394, 105
Gawiser, E., et al. 2006, ApJS, 162, 1
Helou, G., Soifer, B. T., & Rowan-Robinson, M. 1985, ApJ, 298, L7
Huynh, M. T., Jackson, C. A., & Norris, R. P. 2007, AJ, 133, 1331
Huynh, M. T., Jackson, C. A., Norris, R. P., & Prandoni, I. 2005, AJ, 130, 1373
Huynh, M. T., Norris, R. P., Siana, B., & Middelberg, E. 2010, ApJ, 710, 698
Ibar, E., et al. 2008, MNRAS, 386, 953
Lacki, B. C., & Thompson, T. A. 2010, ApJ, 717, 196
Lagache, G., Dole, H., & Puget, J.-L. 2003, MNRAS, 338, 555
Lagache, G., et al. 2004, ApJS, 154, 112
Lilly, S. J., Eales, S. A., Gear, W. K. P., Hammer, F., Le Fèvre, O., Crampton, D., Bond, J. R., & Dunne, L. 1999, ApJ, 518, 641
Lonsdale, C., et al. 2004, ApJS, 154, 54
Lucas, R. A., et al. 2003, AJ, 125, 398
Magnelli, B., Elbaz, D., Chary, R. R., Dickinson, M., Le Borgne, D., Frager, D. T., & Willmer, C. N. A. 2009, A&A, 496, 57
Marchesini, D., van Dokkum, P. G., Förster Schreiber, N. M., Franx, M., Labbé, I., & Wuyts, S. 2009, ApJ, 701, 1765
Marleau, F. R., et al. 2004, ApJS, 154, 66
Middelberg, E., Norris, R. P., Tingay, S., Mao, M. Y., Phillips, C. J., & Hotan, A. W. 2008, A&A, 491, 435
Middelberg, E., et al. 2010, submitted
Murphy, E. J. 2009, ApJ, 706, 482
Murphy, E. J., Chary, R.-R., Alexander, D. M., Dickinson, M., Magnelli, B., Morrison, G., Pope, A., & Teplitz, H. I. 2009, ApJ, 698, 1380
Muzzin, A., van Dokkum, P., Kriek, M., Labbe, I., Cury, I., Marchesini, D., & Franx, M. 2010, arXiv:1003.3479
Norris, R. P., Tingay, S., Phillips, C., Middelberg, E., Deller, A., & Appleton, P. N. 2007, MNRAS, 378, 1434
Norris, R. P., et al. 2006, AJ, 132, 2409
Palunas, P., et al. 2000, ApJ, 541, 61
Papovich, C., et al. 2004, ApJS, 154, 70
Quadri, R., et al. 2007, AJ, 134, 1103
Rieke, G. H., et al. 2004, ApJS, 154, 25
Sargent, M. T., et al. 2010, ApJS, 186, 341
Seymour, N., et al. 2007, ApJS, 171, 353
Seymour, N., Symeonidis, M., Page, M. J., Huynh, M., Dwelly, T., McHardy, I. M., & Rieke, G. 2010, MNRAS, 402, 2666
Shupe, D. L., et al. 2008, AJ, 135, 1050
Werner, M. W., et al. 2004, ApJS, 154, 1
Williams, R. E., et al. 1996, AJ, 112, 1335
Williams, R. E., et al. 2000, AJ, 120, 2735
Yan, L., et al. 2007, ApJ, 658, 778
Yun, M. S., Reddy, N. A., & Condon, J. J. 2001, ApJ, 554, 803